Letter Editors' Suggestion

Competing magnetic states on the surface of multilayer ABC-stacked graphene

Lauro B. Braz,[1,2] Tanay Nag,[2,3] and Annica M. Black-Schaffer[2]

[1]*Instituto de Física, Universidade de São Paulo, Rua do Matão 1371, São Paulo, São Paulo 05508-090, Brazil*
[2]*Department of Physics and Astronomy, Uppsala University, Box 516, S-751 20 Uppsala, Sweden*
[3]*Department of Physics, BITS Pilani-Hyderabad Campus, Telangana 500078, India*

(Received 16 February 2024; accepted 30 October 2024; published 3 December 2024)

We study interaction-mediated magnetism on the surface of ABC-multilayer graphene driven by its zero-energy topological flat bands. Using the random-phase approximation, we treat onsite Hubbard repulsion and find multiple competing magnetic states, due to both intra- and intervalley scattering, with the latter causing an enlarged magnetic unit cell. At half-filling and when the Hubbard repulsion is weak, we observe two different ferromagnetic orders. Once the Hubbard repulsion becomes more realistic, new ferrimagnetic orders arise with distinct incommensurate intra- or intervalley scattering vectors depending on interaction strength and doping, leading to a multitude of competing magnetic states.

DOI: 10.1103/PhysRevB.110.L241401

Introduction. Graphene has extraordinary electronic and structural properties [1–3]. While ideal graphene does not exhibit magnetic properties, various derivatives of graphene do [4–7], e.g., in the presence of a sublattice imbalance [8–11] or due to Landau levels [12–15] or interlayer twists [7,16–21]. In particular, modifications generating flat bands with a high density of states (DOS) close to the Fermi energy are prone to not only magnetism, but generally correlated insulators and even superconductivity [7,22–31]. The flat band dispersion quells kinetic energy, and thus even weak electron-electron interaction generates electronic ordering.

In monolayer graphene, the large Fermi velocity generated by the linear k dispersion prevents electronic ordering. Bilayer AB-stacked (Bernal) and trilayer ABC-stacked (rhombohedral) graphene host quadratic k^2 and cubic k^3 band dispersions, respectively, resulting in electronic instabilities, with bilayer [19,32–38], trilayer [35,36,39–41], and also tetralayer graphene [42,43] having been found to exhibit magnetic, as well as superconducting ordering, but so far only with application of electric and/or magnetic fields [44–49]. Further stacking of N layers in an ABC-sequence produces a locally flat k^N band dispersion on the surfaces of the stack, protected by topology [50–53]. These flat surface states have been shown to host versatile Fermi surface properties [47–49,54–59] leading to magnetism [60–68] and theory proposals also exist for superconductivity, without any need for external fields [31,50,69,70].

Theoretical understanding of ABC-stacked multilayer graphene (ABC-MLG) [49,71] even predating experimental findings, is primarily based on work, including first-principles calculations, studying only the primitive (in-plane) unit cell, then finding surface ferrimagnetism; opposite magnetic moments on the two sublattices with one moment substantially suppressed [62,65–67,69,72,73]. Recent experiments have further reported domain formation [60], interpreted as a competition between a ferrimagnetic state and a suggested correlated paramagnetic state, while longer-range magnetic ordering has only been discussed for finite doping [61]. In this work we study the formation of magnetic ordering on the surface of ABC-MLG, in particular, taking into account all possible magnetic ordering patterns.

We use the T-matrix formalism to isolate the ABC-MLG surface Green's function for $N \gg 1$ layers and then incorporate electronic interactions in the form of Hubbard on-site repulsion U within the matrix random-phase approximation (RPA). We find strong ordering tendencies for both intra- and intervalley scattering, generating single and extended unit cell magnetic patterns, respectively. At half-filling, we find putative ferromagnetic (FM) ordering centered on one sublattice only and mediated by the noninteracting flat bands, but is quickly suppressed for small interactions U. At more realistic U values we find opposite but unequal moments on the two sublattices, rendering ferrimagnetic (FiM) ordering at incommensurate scattering vectors. The intervalley ordering requires lower U for ordering, while the intravalley ordering is close to the commensurate ferrimagnetic order reported in earlier work [61,62,65–67,69,72,73]. Adding finite doping, intravalley ordering instead requires the lowest U, with a substantially shorter spin-spin relaxation time. Our work establishes a fierce competition between different magnetic orders, as well as the importance of incommensurability.

Model and method. To model ABC-MLG we consider a tight-binding model of the bulk unit cell in the basis $\{c_{\tilde{k}}^{A_1}, c_{\tilde{k}}^{B_1}, c_{\tilde{k}}^{A_2}, c_{\tilde{k}}^{B_2}, c_{\tilde{k}}^{A_3}, c_{\tilde{k}}^{B_3}\}$, where $A_n(B_n)$ denotes sublattice A(B) in layer n [57,59]. We use intra(inter)layer hopping $\gamma_1 = 3.3$ eV ($\gamma_2 = 0.42$ eV) between $A_n \to B_n$ ($B_n \to A_{n+1}$), while finite interlayer hopping γ_3 between $A_n \to B_{n+1}$ is responsible for trigonal warping, splitting the graphene Dirac cone into three satellite Dirac cones causing a triangular Fermi surface

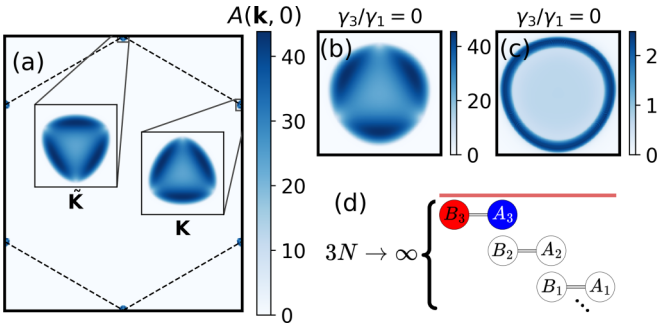

FIG. 1. Surface spectral function $A(\boldsymbol{k}, \omega = 0)$ in the first BZ displaying triangular Fermi surfaces around $\boldsymbol{k} \approx \boldsymbol{K}, \tilde{\boldsymbol{K}}$ for $\gamma_3/\gamma_1 = 0.1$ (a). Structure of $A(\boldsymbol{k} \approx \boldsymbol{K}, \omega = 0)$ for $\mu = 0$ eV (b) and $\mu = 0.025$ eV at $\gamma_3/\gamma_1 = 0$ (c). Surface unit cell with sites $A_1 \cdots B_3$ in three layers with an impurity wall (red line) (d).

[57], using both $\gamma_3/\gamma_1 = 0, 0.1$ for unwarped and warped ABC-MLG. We note that intralayer next nearest neighbor hopping is redundant as satellite Dirac cones already exist. We further use intralayer nearest neighbor distance $a_0 = 1.42$ Å, and interlayer nearest neighbor distance $d_0 = 2.36a_0$ and vary the chemical potential through μ.

As we are interested in the ABC-MLG surface in the limit of $N \gg 1$ layers, we introduce a virtual wall of impurities separating the bulk system into two semi-infinite pieces along the z direction. Following the T-matrix formalism, we construct the surface Green's function $\hat{G}(\tilde{\boldsymbol{k}}_1, \tilde{\boldsymbol{k}}_2, i\omega_n)$ from the bulk Green's function $\hat{G}_0(\tilde{\boldsymbol{k}}, i\omega_n)$ [59,74], with ω_n the Matsubara frequency. We extract the surface Green's function of one of the surfaces adjacent to the impurity plane, $\hat{\mathcal{G}}(\boldsymbol{k}, i\omega_n)$, by partial Fourier transform of $\hat{G}(\tilde{\boldsymbol{k}}_1, \tilde{\boldsymbol{k}}_2, i\omega_n)$ in the z direction, henceforth using the in-plane notation $\boldsymbol{k} = (k_x, k_y)$. This results in an effective surface Green's function for a three layer deep, six carbon atom, single surface unit cell, see schematic in Fig. 1(d). This exact numerical method allows us to encode the effects of a large number of internal layers into $\hat{G}(\tilde{\boldsymbol{k}}_1, \tilde{\boldsymbol{k}}_2, i\omega_n)$ [75]. For more details, see further the Supplemental Material (SM) [76,77].

As a realistic, yet minimal, model of electron-electron interactions, we consider on-site intraorbital Hubbard repulsion $U \sum_{ia} n^a_{i\uparrow} n^a_{i\downarrow}$ where $n^a_{i\sigma} = c^{a\dagger}_{i\sigma} c^a_{i\sigma}$ is the occupation number for site i, orbital a, and spin σ. This interaction is not only the largest term in graphene [78], but nearest-neighbor repulsion is also irrelevant in ABC-MLG since each flat band only occupies one sublattice [61,65,67]. It also reproduces first-principles calculations (of single unit cells) that include the full range of Coulomb interactions [31,69].

We track the influence of interactions on both charge and magnetic fluctuations by employing the RPA to extract the relevant susceptibilities. Magnetic phenomena are governed by the spin susceptibility matrix given by [79–81]

$$\hat{\chi}_s(\boldsymbol{q}, \omega) = \hat{\chi}_0(\boldsymbol{q}, i\omega)[\hat{1} - \hat{U}_s \hat{\chi}_0(\boldsymbol{q}, i\omega)]^{-1}, \tag{1}$$

$$\chi^{sp}_{td}(\boldsymbol{q}, \omega) = -\frac{1}{\beta N} \sum_{\boldsymbol{k}, i\omega_n} \mathcal{G}_{st}(\boldsymbol{k}, i\omega_n) \mathcal{G}_{pd}(\boldsymbol{k} + \boldsymbol{q}, i\omega_n + i\omega), \tag{2}$$

where the noninteracting, or bare, susceptibility matrix $\hat{\chi}_0(\boldsymbol{q}, \omega)$ has size $N_b^2 \times N_b^2$ and is constructed from the surface noninteracting Green's function. $N_b = 6$ denotes the number of carbon sites in the surface unit cell, indexed as $s, p, t, d = A_1, \ldots, B_3$, while $\boldsymbol{q} = (q_x, q_y)$ accounts for the scattering momentum, and $\beta = (k_B T)^{-1}$ is the inverse temperature. The spin interaction matrix $\hat{U}_s$ takes the simple form $U \delta_{sp} \delta_{pt} \delta_{td}$ [80]. To extract magnetically ordered states we use the density-density correlation functions, namely the homogeneous spin susceptibility [82,83], also experimentally tractable [84],

$$\chi(\boldsymbol{q}, \omega) = \frac{1}{2} \sum_{s,p} \chi^{ss}_{pp}(\boldsymbol{q}, \omega). \tag{3}$$

In particular, we compute the real [imaginary] parts of the homogeneous contributions for both the bare susceptibility, $\chi'_0(\boldsymbol{q}, \omega)$ [$\chi''_0(\boldsymbol{q}, \omega)$], and the RPA susceptibility $\chi'_s(\boldsymbol{q}, \omega)$ [$\chi''_s(\boldsymbol{q}, \omega)$]. In a similar treatment for the charge susceptibility, we find that it always remains small compared to the spin susceptibility. We thus conclude that charge fluctuations are not important in ABC-MLG.

A divergent RPA susceptibility signals the formation of an ordered state, for magnetism expressed by the (generalized) Stoner criterion $\det[\tilde{U}_s \hat{\chi}_0(\boldsymbol{q}, \omega) - \lambda \hat{1}] = 0$ with $\tilde{U}_s = \hat{U}_s/U$ [85]. We thus obtain the critical Hubbard interaction strength for magnetic ordering from the maximum positive eigenvalue $\lambda_s^{\boldsymbol{q}_m} = \max\{\lambda_s^{\boldsymbol{q}}\} = 1/U_c^{\boldsymbol{q}_m}$. We perform this analysis over the full first Brillouin zone (BZ) to capture longer-range magnetic ordering patterns, beyond single-unit cell ordering, to include all incommensurate ordering. The eigenvector $\boldsymbol{\psi}^{\omega=0}_{\boldsymbol{q}_m}$, associated with the eigenvalue $\lambda_s^{\boldsymbol{q}_m}$ once the Stoner criterion is satisfied, encodes the spatial structure of the magnetic order [86–90]. Furthermore, a resonance structure in the dynamic profile of $\chi''_s(\boldsymbol{q}_m, \omega)$ at specific $\omega = \tilde{\omega}$ in the ordered regime, i.e., for $U > U_c^{\boldsymbol{q}_m}$, can be assigned as the spin gap of the underlying order [86,87,89]. We further remark that all magnetic states in this work, i.e., within one surface, fall within the layer antiferromagnet (LAF) phase [71] when considering the two opposite surfaces of any slab, see the SM [76].

Flat bands and nesting. We start by analyzing the noninteracting surface states of ABC-MLG. Figure 1(a) shows how the surface spectral function $A(\boldsymbol{k}, \omega = 0)$ acquires substantial weight, signaling a flat band area, around the $\boldsymbol{k} = \boldsymbol{K}, \tilde{\boldsymbol{K}}$ points in a tripartite and triangular shape due to the three satellite Dirac points [57], due to the trigonal warping γ_3. If instead $\gamma_3 = 0$, a circular shape is instead achieved, see Fig. 1(b). Moving away from half-filling, the surface spectral function takes the shape of an annular ring, see Fig. 1(c), now instead capturing the bulk (dispersive) Dirac cones. The surface unit cell with an impurity wall is represented in Fig. 1(d).

The existence of two Fermi surfaces, around $\boldsymbol{K}$ and $\tilde{\boldsymbol{K}}$, leads to both intra- and intervalley scattering with scattering, or nesting, vectors $\boldsymbol{q} \approx \boldsymbol{\Gamma}, \boldsymbol{K}$, respectively. This suggests that more than one type of magnetic order, with different U_c's, may be present. Before investigating magnetic ordering driven by finite interactions, we analyze the effect of nesting on the bare spin susceptibility. In Fig. 2(a) we plot the real static noninteracting susceptibility $\chi'_0(\boldsymbol{q}, \omega = 0)$ at $\mu = 0$ and note large values in small regions $\boldsymbol{\Gamma}_- < \boldsymbol{q} < \boldsymbol{\Gamma}_+$ and $\boldsymbol{K}_- < \boldsymbol{q} < \boldsymbol{K}_+$,

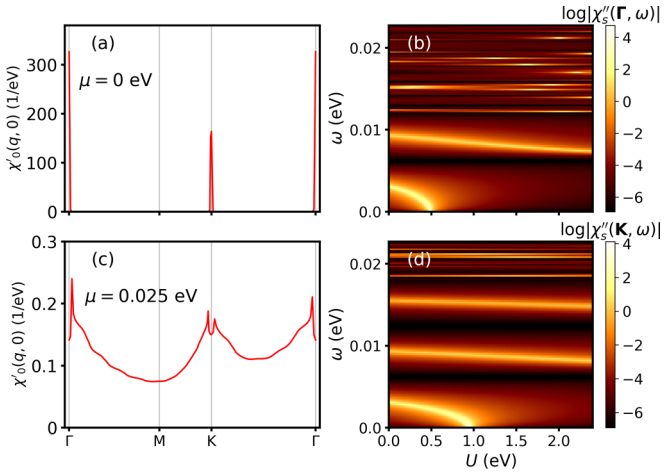

FIG. 2. Real part of the bare spin susceptibility $\chi_0'(\boldsymbol{q}, 0)$ at $\mu = 0$ eV (a) and $\mu = \omega = 0.025$ eV (c) along high-symmetry BZ directions. Imaginary part of the dynamic homogeneous susceptibility $\chi_0''(\boldsymbol{q}, \omega)$ in logarithmic scale in the ω-U plane for $\boldsymbol{q} = \boldsymbol{\Gamma}$ (b), and $\boldsymbol{K}$ (d) for $\mu = 0$ eV. Here $\gamma_3/\gamma_1 = 0.1$.

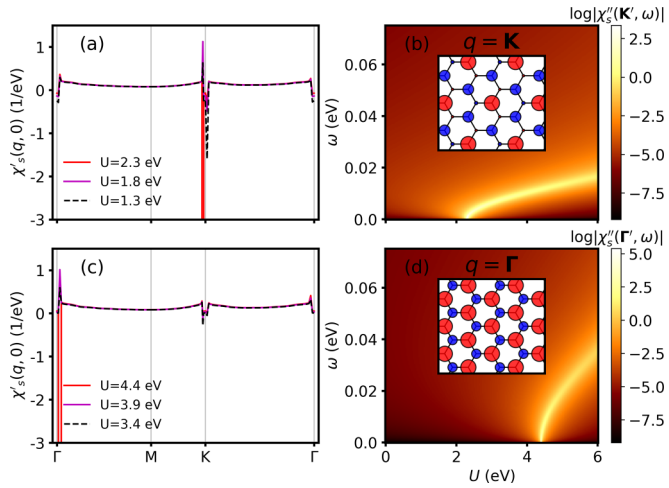

FIG. 3. Real part of the spin susceptibility $\chi_s'(\boldsymbol{q}, 0)$ for $U_c^+ < U \lesssim U_c^{K'}$ (a) and $U_c^{K'} < U \lesssim U_c^{\Gamma'}$ (c) along high-symmetry BZ directions. Imaginary part of the dynamic homogeneous susceptibility $\chi_0''(\boldsymbol{q}, \omega)$ in logarithmic scale in the ω-U plane for $\boldsymbol{q} = \boldsymbol{\Gamma}'$ (b) and $\boldsymbol{q} = \boldsymbol{K}'$ (d). Insets: Real space magnetic structure associated with $\boldsymbol{q} = \boldsymbol{K}'$-, and $\boldsymbol{\Gamma}'$-FiM states on the top surface layer (incommensurability ignored). Circle radii are determined by overall magnet moment magnitudes, colors differentiate signs. Here $\mu = 0$ and $\gamma_3/\gamma_1 = 0.1$.

with divergences at the commensurate nesting vectors $\boldsymbol{q} = \boldsymbol{\Gamma}, \boldsymbol{K}$. The finite regions are due to the finite extent of the surface flat bands. Away from half-filling, $\chi_0'(\boldsymbol{q}, \omega = 0.025)$ instead shows only finite peaks in the same regions, see Fig. 2(b). Thus, divergences in the bare susceptibility are only present due to the zero-energy flat bands and limited to half-filling. This follows directly from the standard representation of the bare homogeneous susceptibility $\chi_0 = \sum_{l,p} \chi_{pp,0}^{ll}(\boldsymbol{q}) \propto \sum_{\boldsymbol{k}} (f(E_l^{\boldsymbol{k}+\boldsymbol{q}}) - f(E_p^{\boldsymbol{k}}))/(\omega + E_l^{\boldsymbol{k}+\boldsymbol{q}} - E_p^{\boldsymbol{k}} + i0^+)$, with $f(E)$ the Fermi-Dirac distribution, where the energy denominator vanishes for the flat bands. We further find no notable dependence on the trigonal warping γ_3.

With a divergent bare spin susceptibility, even an infinitesimal small interaction U triggers magnetic ordering at half-filling according to the generalized Stoner criteria. Analyzing the resulting eigenvectors at $\boldsymbol{\Gamma}$ and $\boldsymbol{K}$, we find magnetic moments only on the top surface's B_3 orbital. For the $\boldsymbol{K}$ ordering, the magnetic moment is also modulated in real space, acquiring zero net magnetization. Due to this magnetic structure, we refer to both of these states as sublattice ferromagnetic (sFM) order and note that they originate from commensurate nesting vectors. To gain more understanding of the sFM orders, we examine the imaginary part of the dynamic bare spin susceptibility $\chi_s''(\boldsymbol{q}, \omega)$ at the divergent scattering vectors $\boldsymbol{q} = \boldsymbol{\Gamma}, \boldsymbol{K}$ in Figs. 2(b) and 2(d) as a function of small U. We find a large (negative) peak starting from $(\omega > 0, U = 0)$ and ending at $(\omega = 0, U = U_c^{\pm})$ with $U_c^- \approx 0.5$ eV for $\boldsymbol{q} = \boldsymbol{\Gamma}$, and $U_c^+ \approx 1.0$ eV for $\boldsymbol{q} = \boldsymbol{K}$. This indicates the existence of a finite spin gap protecting the sFM orders, but only for $U < U_c^{\pm}$. Although the $\boldsymbol{K}$-sFM state has zero magnetization and absence of time-reversal symmetry, the characteristic two-resonance structure of chiral magnons in altermagnets [91,92] is not seen, so this order is unlikely to emerge. For a more in-depth discussion on the sFM orders and their susceptibilities, see the SM [76].

FiM order with interactions. With $U_c^{\pm} \ll \gamma_1$ and estimations of the on-site repulsion in graphene and graphite instead giving $U \gtrsim \gamma_1$ [78,93–95], we do not expect the sFM solutions to likely exist in ABC-MLG. We thus continue analyzing the spin susceptibility $\chi_s(\boldsymbol{q}, \omega)$ for more realistic U, here first at half-filling. We find that as U increases beyond U_c^+, the static spin susceptibility $\chi_s'(\boldsymbol{q}, \omega = 0)$ becomes substantially suppressed at both $\boldsymbol{q} = \boldsymbol{\Gamma}, \boldsymbol{K}$. We instead observe new divergences appearing for intervalley scattering at $\boldsymbol{q} = \boldsymbol{K}' \approx \boldsymbol{K}_-$ with $U_c^{K'} \approx 2.30$ eV and for intravalley scattering at $\boldsymbol{q} = \boldsymbol{\Gamma}' \approx \boldsymbol{\Gamma}_+$ for $U_c^{\Gamma'} \approx 4.40$ eV, see Figs. 3(a) and 3(c). Both divergences appear at incommensurate scattering vectors, linked to the finite extent of the surface flat band and thus different from the noninteracting commensurate sFM states. We can qualitatively understand this shift in scattering vectors by noting that a finite interaction shifts the quasiparticle energies $E_l^{\boldsymbol{k}} \to E_l^{\boldsymbol{k}} + \Sigma_l^{\boldsymbol{k}}$ with a self-energy $\Sigma_l^{\boldsymbol{k}}$ [96], such that the momentum dependence of χ_s may be different from that of χ_0. We further note that the peak in $\chi_s'(\boldsymbol{q}, \omega = 0)$ changes from positive to negative values as soon as the Stoner criterion is satisfied at $U_c^{\Gamma', K'}$ [86,87,89]. The negatively valued divergency is necessary due to the previous magnetic transitions at $U < U_c^{\Gamma', K'}$ found in the previous section, see the SM [76].

In terms of the resulting magnetic moments for the $\boldsymbol{\Gamma}'$ state, we find that the dominant contribution to $\chi_s'(\boldsymbol{q}, 0)$ comes from the top surface B_3 orbital and now also with the A_3 orbital carrying an unequal finite magnetic moment but with opposite sign, as illustrated in the inset of Fig. 3(d) (incommensurability not visible). A similar analysis of the $\boldsymbol{K}'$ state results in the pattern in the inset of Fig. 3(b), again with dominant contribution from a B_3 orbital, but now with a $\sqrt{3} \times \sqrt{3}$ extended spatial repetition, due to the intervalley scattering [86–88], see the SM [76]. Due to these patterns, we refer to the $\boldsymbol{\Gamma}'$ and $\boldsymbol{K}'$ states as incommensurate ferrimagnetic (FiM) orders, but note that the latter can also be called an incommensurate spin density wave.

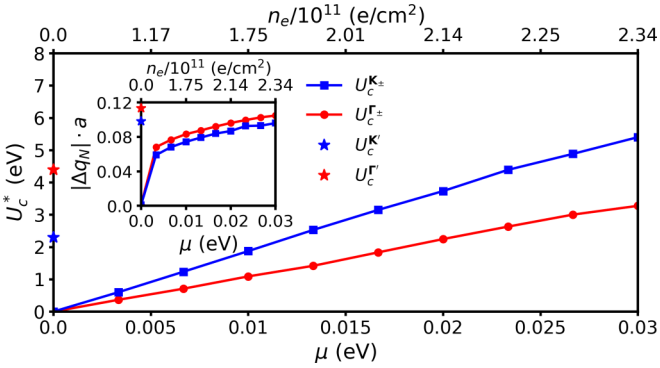

FIG. 4. Minimum critical Hubbard interaction U_c^* extracted for all scattering vectors in a circular region around $\boldsymbol{\Gamma}$ (red) and $\boldsymbol{K}$ (blue) as a function of doping μ and carrier density n_e. (Inset) Deviation in the ordering vectors with respect to the high-symmetry points $\Delta\boldsymbol{q}_N = \boldsymbol{\Gamma}''(\boldsymbol{K}'') - \boldsymbol{\Gamma}(\boldsymbol{K})$ normalized by the real-space graphene lattice constant a as a function of μ and carrier density n_e. Stars indicate $U_c^{\Gamma'}$, $U_c^{K'}$, and deviation for $\boldsymbol{\Gamma}'$, $\boldsymbol{K}'$ in the main plot and inset, respectively. Corresponding number density (units of e/cm^2) on the upper horizontal axes (not linear scale). Here $\gamma_3/\gamma_1 = 0.1$.

Moreover, we consider the dynamic profile of $\chi_s''(\boldsymbol{q},\omega)$ in Figs. 3(b) and 3(d), now at the incommensurate wave vectors $\boldsymbol{q} = \boldsymbol{\Gamma}', \boldsymbol{K}'$ hosting the divergent (real) spin susceptibility [97]. We find a large positive peak originating at $U = U_c^{\Gamma',K'}$ and $\omega = 0$ and rising to larger frequencies ω with increasing U. This signals the existence of finite spin gaps [83,84], confirming the formation of first a $\boldsymbol{K}'$-FiM state at $U_c^{K'}$ from intervalley scattering and then a $\boldsymbol{\Gamma}'$-FiM ordered state at $U_c^{\Gamma'}$ from intravalley scattering. With the spin susceptibility at $\boldsymbol{K}'$ becoming substantially suppressed at $U_c^{\Gamma'}$, see Fig. 3(c), we infer that the $\boldsymbol{\Gamma}'$-FiM order likely directly set in at $U > U_c^{\Gamma'}$ with little competition from the $\boldsymbol{K}'$-FiM order, see the SM [76]. We further find that $\boldsymbol{\Gamma}', \boldsymbol{K}'$ varies slightly with trigonal warping, producing slightly different U_c's, but not changing the overall behavior. Taken together, these results point to a close competition between the $\boldsymbol{\Gamma}'$-FiM and $\boldsymbol{K}'$-FiM states at half-filling, such that any spatial dependence of U will likely create spontaneous domains of different FiM states.

Finite doping. Finally, we vary the doping away from half-filling, modeling spontaneous charge inhomogeneity [61] or an applied gate voltage [60,61]. To probe the doping dependence, we extract the minimum critical Hubbard parameter U_c^* at zero temperature, satisfying the Stoner criterion for any nesting vector $\boldsymbol{q}$ in disks centered at $\boldsymbol{\Gamma}, \boldsymbol{K}$ to capture all previously explored divergences and beyond. In Fig. 4 we plot the result as a function of doping μ (lower-horizontal axis) with associated number density n_e (upper-horizontal axis). We find increasing U_c^* for both intravalley (red) and intervalley scattering (blue), with higher U_c^* for the latter. At $\mu = 0$ eV the results coincide with Fig. 2 with its commensurate orders already at $U_c^* = 0$. With increasing doping, we find a roughly linear increase in U_c^*, while at the same time, the ordering vectors move away from $\boldsymbol{\Gamma}, \boldsymbol{K}$. The resulting scattering vectors are labeled $\boldsymbol{\Gamma}''$ and $\boldsymbol{K}''$, and the order as $\boldsymbol{\Gamma}''$- and $\boldsymbol{K}''$-FiM orders as they show large similarities with the $\mu = 0$ FiM orders, see the SM [76].

We plot the deviation $\Delta q_\Gamma = |\boldsymbol{\Gamma}'' - \boldsymbol{\Gamma}|$ and similar for $\boldsymbol{K}$ in the inset of Fig. 4. There is a sharp jump in Δq directly when μ acquires finite value, followed by a slow increase for increasing μ. We find that $\Delta q_{\Gamma,K}$ fully tracks the position of the finite amplitude peaks in the bare susceptibility, see Fig. 2(c) for a fixed μ. Thus, magnetic ordering at finite doping is fully determined by the bare susceptibility with the interaction just enhancing its peaks into divergences at U_c^*. This is notably different from the half-filled case where the interaction also shifts the ordering vectors to incommensurate vectors, compare Figs. 2(a), 3(a) and 3(c).

To highlight further differences to the half-filling results in Fig. 3, we mark $U_c^{\Gamma',K'}$ with stars in Fig. 4. As seen, at half-filling, intervalley FiM order commands the lowest U_c, while at any finite doping, intravalley scattering has the lowest U_c. Also, the incommensurability is always largest at half-filling, which seems to provide an upper limit for $\Delta\boldsymbol{q}$ at finite doping. We also find a notably different overall behavior of the spin susceptibility. At half-filling a clear spin gap is present at $U = 0$, protecting the commensurate sFM orders until its closure at $U_c^{\pm}$, while at $U_c^{\Gamma',K'}$, a new spin gap develops, protecting the FiM orders as shown in Figs. 2(b), 2(d), 3(b) and 3(d). Instead, at finite doping no spin gap, or order, exists for any $U < U_c^*$. Moreover, when ordering is established at U_c^*, we find no sharp peaks at finite frequencies in χ_s''. The dynamic susceptibility displays signatures of a markedly short spin-spin relaxation time [91,98,99], flattening the peaks in χ'' and also making χ' continuous at nonzero frequencies. We attribute the shortened relaxation time to more substantial overlap with the dispersive surface states at finite doping [91], generating damping. Interestingly, the bulk metallic states do not generate any strong damping, as obvious from orders at half-filling. Still tracing a spin gap from the (flattened) peaks in χ_s'', we find that they never disappear with increasing U, once developed at U_c^*. For more information, see the SM [76]. Based on the different U_cs and their trends, scattering vectors, and different relaxation times, we conclude that the states at finite doping are notably different from those at half-filling.

Concluding remarks. Our work reveals how the surface flat band in ABC-multilayer graphene leads to a plethora of magnetic states: at half-filling, commensurate sFM orders with either intra- and intervalley nesting vectors in the noninteracting limit, but at any realistic interaction strength, incommensurate FiM orders instead develop for both intra- and intervalley scattering. Away from half-filling, interactions result in another set of incommensurate FiM orders with different nesting vectors and a shorter spin-spin relaxation time. This demonstrates remarkably rich possibilities for different magnetic ordering on the surface ABC-MLG: both competing intra- and intervalley scattering and with ordering varying intricately as a function of interaction and doping [91,92].

We note that there exist qualitative similarities between our results on ABC-MLG with $N \gg 1$ layers and recent experiments on few-layer graphene. For example, all our magnetic states belong to the layer antiferromagnet (LAF) phase recently found in pentalayer ABC-stacked graphene [68,71], but we additionally uncover a rich in-surface structure for these LAF states. Also, in contrast to bilayer [32–34,38], trilayer [39–41], tetralayer [42,43], and pentalayer [68] graphene, external displacement field is not required to stabilize magnetic

states in ABC-MLG. The reduced spin-spin relaxation time with finite doping also agrees with the loss of magnetic ordering in fewer-layer systems. Further, recent experimental work on ABC-MLG has reported a gapped magnetic order at half-filling and an enlarged magnetic unit cell at finite doping, similar to our $\boldsymbol{\Gamma}'$- and $\boldsymbol{K}'$-FiM states, respectively, but without incommensurability, together with an ungapped phase modeled as a correlated paramagnetic phase [61]. Importantly, we find that both incommensurability and magnetic pattern vary intricately with interaction strength and doping, resulting in a multitude of energetically close but different domains in real samples. This likely results in increased quantum fluctuations and reduced energy gaps, consistent with current experiments [60,61].

Acknowledgments. We thank G.B. Martins for insights on the RPA method, P. Holmvall for providing his code implementation of the Matsubara summations, and X. Feng, D. Chakraborty, R. Arouca, P. M. Oppeneer, and P. Thundström for fruitful discussions. We acknowledge financial support from the Knut and Alice Wallenberg Foundation through the Wallenberg Academy Fellows program and Project Grant KAW 2019.0068, Coordenação de Aperfeiçoamento de Pessoal de Nível Superior - Brasil (CAPES) - Finance Code 001, FAPESP (Grant No. 2023/14902-8).

[1] A. K. Geim and K. S. Novoselov, The rise of graphene, Nat. Mater. **6**, 183 (2007).

[2] A. H. Castro Neto, F. Guinea, N. M. R. Peres, K. S. Novoselov, and A. K. Geim, The electronic properties of graphene, Rev. Mod. Phys. **81**, 109 (2009).

[3] K. S. Novoselov, A. K. Geim, S. V. Morozov, D. Jiang, Y. Zhang, S. V. Dubonos, I. V. Grigorieva, and A. A. Firsov, Electric field effect in atomically thin carbon films, Science **306**, 666 (2004).

[4] J. Fernández-Rossier and J. J. Palacios, Magnetism in graphene nanoislands, Phys. Rev. Lett. **99**, 177204 (2007).

[5] Y.-W. Son, M. L. Cohen, and S. G. Louie, Energy gaps in graphene nanoribbons, Phys. Rev. Lett. **97**, 216803 (2006).

[6] O. V. Yazyev, Emergence of magnetism in graphene materials and nanostructures, Rep. Prog. Phys. **73**, 056501 (2010).

[7] A. L. Sharpe, E. J. Fox, A. W. Barnard, J. Finney, K. Watanabe, T. Taniguchi, M. A. Kastner, and D. Goldhaber-Gordon, Emergent ferromagnetism near three-quarters filling in twisted bilayer graphene, Science **365**, 605 (2019).

[8] P. Esquinazi, D. Spemann, R. Höhne, A. Setzer, K.-H. Han, and T. Butz, Induced magnetic ordering by proton irradiation in graphite, Phys. Rev. Lett. **91**, 227201 (2003).

[9] J. J. Palacios, J. Fernández-Rossier, and L. Brey, Vacancy-induced magnetism in graphene and graphene ribbons, Phys. Rev. B **77**, 195428 (2008).

[10] G. Z. Magda, X. Jin, I. Hagymási, P. Vancsó, Z. Osváth, P. Nemes-Incze, C. Hwang, L. P. Biró, and L. Tapasztó, Room-temperature magnetic order on zigzag edges of narrow graphene nanoribbons, Nature (London) **514**, 608 (2014).

[11] Y. Lemonik, I. Aleiner, and V. I. Fal'ko, Competing nematic, antiferromagnetic, and spin-flux orders in the ground state of bilayer graphene, Phys. Rev. B **85**, 245451 (2012).

[12] E. McCann and V. I. Fal'ko, Landau-level degeneracy and quantum Hall effect in a graphite bilayer, Phys. Rev. Lett. **96**, 086805 (2006).

[13] K. Nomura and A. H. MacDonald, Quantum Hall ferromagnetism in graphene, Phys. Rev. Lett. **96**, 256602 (2006).

[14] M. O. Goerbig, Electronic properties of graphene in a strong magnetic field, Rev. Mod. Phys. **83**, 1193 (2011).

[15] A. F. Young, J. D. Sanchez-Yamagishi, B. Hunt, S. H. Choi, K. Watanabe, T. Taniguchi, R. C. Ashoori, and P. Jarillo-Herrero, Tunable symmetry breaking and helical edge transport in a graphene quantum spin Hall state, Nature (London) **505**, 528 (2014).

[16] R. Bistritzer and A. H. MacDonald, Moiré bands in twisted double-layer graphene, Proc. Natl. Acad. Sci. USA **108**, 12233 (2011).

[17] G. Chen, A. L. Sharpe, E. J. Fox, Y.-H. Zhang, S. Wang, L. Jiang, B. Lyu, H. Li, K. Watanabe, T. Taniguchi, Z. Shi, T. Senthil, D. Goldhaber-Gordon, Y. Zhang, and F. Wang, Tunable correlated Chern insulator and ferromagnetism in a moiré superlattice, Nature (London) **579**, 56 (2020).

[18] L. Klebl, Z. A. H. Goodwin, A. A. Mostofi, D. M. Kennes, and J. Lischner, Importance of long-ranged electron-electron interactions for the magnetic phase diagram of twisted bilayer graphene, Phys. Rev. B **103**, 195127 (2021).

[19] L. A. Gonzalez-Arraga, J. L. Lado, F. Guinea, and P. San-Jose, Electrically controllable magnetism in twisted bilayer graphene, Phys. Rev. Lett. **119**, 107201 (2017).

[20] X. Y. Xu, K. T. Law, and P. A. Lee, Kekulé valence bond order in an extended Hubbard model on the honeycomb lattice with possible applications to twisted bilayer graphene, Phys. Rev. B **98**, 121406(R) (2018).

[21] J. Liu, Z. Ma, J. Gao, and X. Dai, Quantum valley Hall effect, orbital magnetism, and anomalous Hall effect in twisted multilayer graphene systems, Phys. Rev. X **9**, 031021 (2019).

[22] Y. Cao, V. Fatemi, S. Fang, K. Watanabe, T. Taniguchi, E. Kaxiras, and P. Jarillo-Herrero, Unconventional superconductivity in magic-angle graphene superlattices, Nature (London) **556**, 43 (2018).

[23] X. Lu, P. Stepanov, W. Yang, M. Xie, M. A. Aamir, I. Das, C. Urgell, K. Watanabe, T. Taniguchi, G. Zhang, A. Bachtold, A. H. MacDonald, and D. K. Efetov, Superconductors, orbital magnets and correlated states in magic-angle bilayer graphene, Nature (London) **574**, 653 (2019).

[24] Y. Xie, B. Lian, B. Jäck, X. Liu, C.-L. Chiu, K. Watanabe, T. Taniguchi, B. A. Bernevig, and A. Yazdani, Spectroscopic signatures of many-body correlations in magic-angle twisted bilayer graphene, Nature (London) **572**, 101 (2019).

[25] H. C. Po, L. Zou, A. Vishwanath, and T. Senthil, Origin of Mott insulating behavior and superconductivity in twisted bilayer graphene, Phys. Rev. X **8**, 031089 (2018).

[26] G. Li, A. Luican, J. M. B. Lopes dos Santos, A. H. Castro Neto, A. Reina, J. Kong, and E. Y. Andrei, Observation of Van Hove singularities in twisted graphene layers, Nat. Phys. **6**, 109 (2010).

[27] Y. Choi, J. Kemmer, Y. Peng, A. Thomson, H. Arora, R. Polski, Y. Zhang, H. Ren, J. Alicea, G. Refael, F. von Oppen,

K. Watanabe, T. Taniguchi, and S. Nadj-Perge, Electronic correlations in twisted bilayer graphene near the magic angle, Nat. Phys. **15**, 1174 (2019).

[28] Y. Cao, V. Fatemi, A. Demir, S. Fang, S. L. Tomarken, J. Y. Luo, J. D. Sanchez-Yamagishi, K. Watanabe, T. Taniguchi, E. Kaxiras, R. C. Ashoori, and P. Jarillo-Herrero, Correlated insulator behaviour at half-filling in magic-angle graphene superlattices, Nature (London) **556**, 80 (2018).

[29] Y. Jiang, X. Lai, K. Watanabe, T. Taniguchi, K. Haule, J. Mao, and E. Y. Andrei, Charge order and broken rotational symmetry in magic-angle twisted bilayer graphene, Nature (London) **573**, 91 (2019).

[30] E. Y. Andrei and A. H. MacDonald, Graphene bilayers with a twist, Nat. Mater. **19**, 1265 (2020).

[31] T. Löthman and A. M. Black-Schaffer, Universal phase diagrams with superconducting domes for electronic flat bands, Phys. Rev. B **96**, 064505 (2017).

[32] J. Velasco, L. Jing, W. Bao, Y. Lee, P. Kratz, V. Aji, M. Bockrath, C. N. Lau, C. Varma, R. Stillwell, D. Smirnov, F. Zhang, J. Jung, and A. H. MacDonald, Transport spectroscopy of symmetry-broken insulating states in bilayer graphene, Nat. Nanotechnol. **7**, 156 (2012).

[33] F. R. Geisenhof, F. Winterer, A. M. Seiler, J. Lenz, T. Xu, F. Zhang, and R. T. Weitz, Quantum anomalous Hall octet driven by orbital magnetism in bilayer graphene, Nature (London) **598**, 53 (2021).

[34] H. Zhou, L. Holleis, Y. Saito, L. Cohen, W. Huynh, C. L. Patterson, F. Yang, T. Taniguchi, K. Watanabe, and A. F. Young, Isospin magnetism and spin-polarized superconductivity in Bernal bilayer graphene, Science **375**, 774 (2022).

[35] E. Pangburn, L. Haurie, A. Crépieux, O. A. Awoga, A. M. Black-Schaffer, C. Pépin, and C. Bena, Superconductivity in monolayer and few-layer graphene. I. Review of possible pairing symmetries and basic electronic properties, Phys. Rev. B **108**, 134514 (2023).

[36] A. Crépieux, E. Pangburn, L. Haurie, O. A. Awoga, A. M. Black-Schaffer, N. Sedlmayr, C. Pépin, and C. Bena, Superconductivity in monolayer and few-layer graphene. II. Topological edge states and Chern numbers, Phys. Rev. B **108**, 134515 (2023).

[37] P. A. Pantaleón, A. Jimeno-Pozo, H. S.-Cruz, V. Tiê′n Phong, T. Cea, and F. Guinea, Superconductivity and correlated phases in non-twisted bilayer and trilayer graphene, Nat. Rev. Phys. **5**, 304 (2023).

[38] D. Marchenko, D. V. Evtushinsky, E. Golias, A. Varykhalov, Th. Seyller, and O. Rader, Extremely flat band in bilayer graphene, Sci. Adv. **4**, eaau0059 (2018).

[39] Y. Lee, D. Tran, K. Myhro, J. Velasco, N. Gillgren, C. N. Lau, Y. Barlas, J. M. Poumirol, D. Smirnov, and F. Guinea, Competition between spontaneous symmetry breaking and single-particle gaps in trilayer graphene, Nat. Commun. **5**, 5656 (2014).

[40] M. Yankowitz, J. I.-J. Wang, A. G. Birdwell, Y.-A. Chen, K. Watanabe, T. Taniguchi, P. Jacquod, P. San-Jose, P. Jarillo-Herrero, and B. J. LeRoy, Electric field control of soliton motion and stacking in trilayer graphene, Nat. Mater. **13**, 786 (2014).

[41] H. Zhou, T. Xie, T. Taniguchi, K. Watanabe, and A. F. Young, Superconductivity in rhombohedral trilayer graphene, Nature (London) **598**, 434 (2021).

[42] K. Myhro, S. Che, Y. Shi, Y. Lee, K. Thilahar, K. Bleich, D. Smirnov, and C. N. Lau, Large tunable intrinsic gap in rhombohedral-stacked tetralayer graphene at half filling, 2D Mater. **5**, 045013 (2018).

[43] A. Kerelsky, C. Rubio-Verdú, L. Xian, D. M. Kennes, D. Halbertal, N. Finney, L. Song, S. Turkel, L. Wang, K. Watanabe, T. Taniguchi, J. Hone, C. Dean, D. N. Basov, A. Rubio, and A. N. Pasupathy, Moiréless correlations in ABCA graphene, Proc. Natl. Acad. Sci. USA **118**, e2017366118 (2021).

[44] A. A. Avetisyan, B. Partoens, and F. M. Peeters, Electric-field control of the band gap and fermi energy in graphene multilayers by top and back gates, Phys. Rev. B **80**, 195401 (2009).

[45] H. Min, B. Sahu, S. K. Banerjee, and A. H. MacDonald, Ab initio theory of gate induced gaps in graphene bilayers, Phys. Rev. B **75**, 155115 (2007).

[46] P. Gava, M. Lazzeri, A. M. Saitta, and F. Mauri, Ab initio study of gap opening and screening effects in gated bilayer graphene, Phys. Rev. B **79**, 165431 (2009).

[47] M. Koshino, Interlayer screening effect in graphene multilayers with ABA and ABC stacking, Phys. Rev. B **81**, 125304 (2010).

[48] C. H. Lui, Z. Li, K. F. Mak, E. Cappelluti, and T. F. Heinz, Observation of an electrically tunable band gap in trilayer graphene, Nat. Phys. **7**, 944 (2011).

[49] F. Zhang, B. Sahu, H. Min, and A. H. MacDonald, Band structure of ABC-stacked graphene trilayers, Phys. Rev. B **82**, 035409 (2010).

[50] T. T. Heikkilä, N. B. Kopnin, and G. E. Volovik, Flat bands in topological media, JETP Lett. **94**, 233 (2011).

[51] T. T. Heikkilä and G. E. Volovik, Dimensional crossover in topological matter: Evolution of the multiple Dirac point in the layered system to the flat band on the surface, JETP Lett. **93**, 59 (2011).

[52] J. W. McClure, Electron energy band structure and electronic properties of rhombohedral graphite, Carbon **7**, 425 (1969).

[53] H. Henck, J. Avila, Z. Ben Aziza, D. Pierucci, J. Baima, B. Pamuk, J. Chaste, D. Utt, M. Bartos, K. Nogajewski, B. A. Piot, M. Orlita, M. Potemski, M. Calandra, M. C. Asensio, F. Mauri, C. Faugeras, and A. Ouerghi, Flat electronic bands in long sequences of rhombohedral-stacked graphene, Phys. Rev. B **97**, 245421 (2018).

[54] H. Min and A. H. MacDonald, Chiral decomposition in the electronic structure of graphene multilayers, Phys. Rev. B **77**, 155416 (2008).

[55] S. Yuan, R. Roldán, and M. I. Katsnelson, Landau level spectrum of ABA- and ABC-stacked trilayer graphene, Phys. Rev. B **84**, 125455 (2011).

[56] W. Bao, L. Jing, J. Velasco, Y. Lee, G. Liu, D. Tran, B. Standley, M. Aykol, S. B. Cronin, D. Smirnov, M. Koshino, E. McCann, M. Bockrath, and C. N. Lau, Stacking-dependent band gap and quantum transport in trilayer graphene, Nat. Phys. **7**, 948 (2011).

[57] J. Jung and A. H. MacDonald, Gapped broken symmetry states in abc-stacked trilayer graphene, Phys. Rev. B **88**, 075408 (2013).

[58] Z. Gao, S. Wang, J. Berry, Q. Zhang, J. Gebhardt, W. M. Parkin, J. Avila, H. Yi, C. Chen, S. Hurtado-Parra, M. Drndić, A. M. Rappe, D. J. Srolovitz, J. M. Kikkawa, Z. Luo, M. C. Asensio, F. Wang, and A. T. Charlie Johnson, Large-area epitaxial growth of curvature-stabilized ABC trilayer graphene, Nat. Commun. **11**, 546 (2020).

[59] V. Kaladzhyan, S. Pinon, Frédéric Joucken, Z. Ge, E. A. Quezada-Lopez, T. Taniguchi, K. Watanabe, J. Velasco, and C. Bena, Surface states and quasiparticle interference in bernal and rhombohedral graphite with and without trigonal warping, Phys. Rev. B **104**, 155418 (2021).

[60] Y. Shi, S. Xu, Y. Yang, S. Slizovskiy, S. V. Morozov, S.-K. Son, S. Ozdemir, C. Mullan, J. Barrier, J. Yin, A. I. Berdyugin, B. A. Piot, T. Taniguchi, K. Watanabe, V. I. Fal'ko, K. S. Novoselov, A. K. Geim, and A. Mishchenko, Electronic phase separation in multilayer rhombohedral graphite, Nature (London) **584**, 210 (2020).

[61] I. Hagymási, M. S. Mohd Isa, Z. Tajkov, K. Márity, L. Oroszlány, J. Koltai, A. Alassaf, P. Kun, K. Kandrai, A. Pálinkás, P. Vancsó, L. Tapasztó, and P. Nemes-Incze, Observation of competing, correlated ground states in the flat band of rhombohedral graphite, Sci. Adv. **8**, eabo6879 (2022).

[62] B. Pamuk, J. Baima, F. Mauri, and M. Calandra, Magnetic gap opening in rhombohedral-stacked multilayer graphene from first principles, Phys. Rev. B **95**, 075422 (2017).

[63] Y. Henni, H. P. Ojeda Collado, K. Nogajewski, M. R. Molas, G. Usaj, C. A. Balseiro, M. Orlita, M. Potemski, and C. Faugeras, Rhombohedral multilayer graphene: A magneto-Raman scattering study, Nano Lett. **16**, 3710 (2016).

[64] Y. Lee, S. Che, J. Velasco, Jr., X. Gao, Y. Shi, D. Tran, J. Baima, F. Mauri, M. Calandra, M. Bockrath, and C. N. Lau, Gate-tunable magnetism and giant magnetoresistance in suspended rhombohedral-stacked few-layer Graphene, Nano Lett. **22**, 5094 (2022).

[65] M. Otani, M. Koshino, Y. Takagi, and S. Okada, Intrinsic magnetic moment on (0001) surfaces of rhombohedral graphite, Phys. Rev. B **81**, 161403 (2010).

[66] R. Xiao, F. Tasnádi, K. Koepernik, J. W. F. Venderbos, M. Richter, and M. Taut, Density functional investigation of rhombohedral stacks of graphene: Topological surface states, nonlinear dielectric response, and bulk limit, Phys. Rev. B **84**, 165404 (2011).

[67] N. T. Cuong, M. Otani, and S. Okada, Magnetic-state tuning of the rhombohedral graphite film by interlayer spacing and thickness, Surf. Sci. **606**, 253 (2012).

[68] T. Han, Z. Lu, G. Scuri, J. Sung, J. Wang, T. Han, K. Watanabe, T. Taniguchi, H. Park, and L. Ju, Correlated insulator and Chern insulators in pentalayer rhombohedral-stacked graphene, Nat. Nanotechnol. **19**, 181 (2024).

[69] O. A. Awoga, T. Löthman, and A. M. Black-Schaffer, Superconductivity and magnetism in the surface states of ABC-stacked multilayer graphene, Phys. Rev. B **108**, 144504 (2023).

[70] N. B. Kopnin, T. T. Heikkilä, and G. E. Volovik, High-temperature surface superconductivity in topological flat-band systems, Phys. Rev. B **83**, 220503(R) (2011).

[71] F. Zhang, J. Jung, G. A. Fiete, Q. Niu, and A. H. MacDonald, Spontaneous quantum Hall states in chirally stacked few-layer graphene systems, Phys. Rev. Lett. **106**, 156801 (2011).

[72] D.-H. Xu, J. Yuan, Z.-J. Yao, Y. Zhou, J.-H. Gao, and F.-C. Zhang, Stacking order, interaction, and weak surface magnetism in layered graphene sheets, Phys. Rev. B **86**, 201404(R) (2012).

[73] R. Olsen, R. van Gelderen, and C. Morais Smith, Ferromagnetism in ABC-stacked trilayer graphene, Phys. Rev. B **87**, 115414 (2013).

[74] S. Pinon, V. Kaladzhyan, and C. Bena, Surface Green's functions and boundary modes using impurities: Weyl semimetals and topological insulators, Phys. Rev. B **101**, 115405 (2020).

[75] We verify that the surface spectral function, $A(\boldsymbol{k},\omega) = -\mathrm{Im}[\mathrm{Tr}[\sum_{i\omega_n}\hat{\mathcal{G}}(\boldsymbol{k},z_1,z_2,i\omega_n+\omega)]/\pi]$, reproduces the surface flat bands [59].

[76] See Supplemental Material at http://link.aps.org/supplemental/10.1103/PhysRevB.110.L241401 for discussions on surface Green's function formalism, static spin susceptibility profile, dynamic spin susceptibility at half-filling, as well as away from half-filling and magnetic spin textures.

[77] T. Ozaki, Continued fraction representation of the Fermi-Dirac function for large-scale electronic structure calculations, Phys. Rev. B **75**, 035123 (2007).

[78] T. O. Wehling, E. Şaşıoğlu, C. Friedrich, A. I. Lichtenstein, M. I. Katsnelson, and S. Blügel, Strength of effective Coulomb interactions in graphene and graphite, Phys. Rev. Lett. **106**, 236805 (2011).

[79] D. J. Scalapino, E. Loh, Jr., and J. E. Hirsch, d-wave pairing near a spin-density-wave instability, Phys. Rev. B **34**, 8190(R) (1986).

[80] S. Graser, T. A. Maier, P. J. Hirschfeld, and D. J. Scalapino, Near-degeneracy of several pairing channels in multiorbital models for the Fe pnictides, New J. Phys. **11**, 025016 (2009).

[81] A. F. Kemper, T. A. Maier, S. Graser, H.-P. Cheng, P. J. Hirschfeld, and D. J. Scalapino, Sensitivity of the superconducting state and magnetic susceptibility to key aspects of electronic structure in ferropnictides, New J. Phys. **12**, 073030 (2010).

[82] G. D. Mahan, *Many-Particle Physics* (Springer US, Boston, MA, 2000).

[83] H. Bruus and K. Flensberg, *Many-Body Quantum Theory in Condensed Matter Physics: An Introduction*, Oxford Graduate Texts (Oxford University Press, Oxford, New York, 2004).

[84] A. Kreisel, P. J. Hirschfeld, and B. M. Andersen, Theory of spin-excitation anisotropy in the nematic phase of FeSe obtained from RIXS measurements, Front. Phys. **10**, 859424 (2022).

[85] H. Sakakibara, H. Usui, K. Kuroki, R. Arita, and H. Aoki, Origin of the material dependence of T_c in the single-layered cuprates, Phys. Rev. B **85**, 064501 (2012).

[86] H. F. Fong, P. Bourges, Y. Sidis, L. P. Regnault, J. Bossy, A. Ivanov, D. L. Milius, I. A. Aksay, and B. Keimer, Spin susceptibility in underdoped $YBa_2Cu_3O_{6+x}$, Phys. Rev. B **61**, 14773 (2000).

[87] Y. Gao, T. Zhou, C. S. Ting, and W.-P. Su, Spin dynamics in electron-doped iron pnictide superconductors, Phys. Rev. B **82**, 104520 (2010).

[88] L. V. Boehnke, Susceptibilities in materials with multiple strongly correlated orbitals, Ph.D. thesis, Universität Hamburg, Hamburg 2015.

[89] M. H. Christensen, H. Jacobsen, T. A. Maier, and B. M. Andersen, Magnetic fluctuations in pair-density-wave superconductors, Phys. Rev. Lett. **116**, 167001 (2016).

[90] A. Fischer, Z. A. H. Goodwin, A. A. Mostofi, J. Lischner, D. M. Kennes, and L. Klebl, Unconventional superconductivity in magic-angle twisted trilayer graphene, npj Quantum Mater. **7**, 5 (2022).

[91] T. A. Maier and S. Okamoto, Weak-coupling theory of neutron scattering as a probe of altermagnetism, Phys. Rev. B **108**, L100402 (2023).

[92] L. Šmejkal, A. Marmodoro, K.-H. Ahn, R. González-Hernández, I. Turek, S. Mankovsky, H. Ebert, S. W. D'Souza, O. Šipr, J. Sinova, and T. Jungwirth, Chiral magnons in altermagnetic RuO_2, Phys. Rev. Lett. **131**, 256703 (2023).

[93] N. Tancogne-Dejean and A. Rubio, Parameter-free hybridlike functional based on an extended Hubbard model: DFT + U + V, Phys. Rev. B **102**, 155117 (2020).

[94] R. J. Bursill, C. Castleton, and W. Barford, Optimal parametrisation of the Pariser–Parr–Pople Model for benzene and biphenyl, Chem. Phys. Lett. **294**, 305 (1998).

[95] J. A. Vergés, E. SanFabián, G. Chiappe, and E. Louis, Fit of Pariser-Parr-Pople and Hubbard model Hamiltonians to charge and spin states of polycyclic aromatic hydrocarbons, Phys. Rev. B **81**, 085120 (2010).

[96] N. F. Berk and J. R. Schrieffer, Effect of ferromagnetic spin correlations on superconductivity, Phys. Rev. Lett. **17**, 433 (1966).

[97] The change to incommensurate wave vectors means the peaks in Figs. 2(b) and 2(c) at small U for commensurate vectors are not visible in Figs. 3(b) and 3(d).

[98] A. L. Barra and A. K. Hassan, Electron spin resonance, in *Encyclopedia of Condensed Matter Physics*, edited by F. Bassani, G. L. Liedl, and P. Wyder (Elsevier, Oxford, 2005) pp. 58–67.

[99] O. Yalçın, Ferromagnetic Resonance, in *Ferromagnetic Resonance - Theory and Applications* (IntechOpen, London, UK, 2013).